Published OnlineFirst May 16, 2019; DOI: 10.1158/0008-5472.CAN-18-3769

Convergence and Technologies

Cancer Research

Volumetric Optoacoustic Imaging Unveils High-Resolution Patterns of Acute and Cyclic Hypoxia in a Murine Model of Breast Cancer

Avihai Ron[1,2], Xosé Luís Deán-Ben[1,3,4], Sven Gottschalk[1], and Daniel Razansky[1,2,3,4]

Abstract

Mapping tumor heterogeneity and hypoxia within a living intact organism is essential for understanding the processes involved in cancer progression and assessing long-term responses to therapies. Efficient investigations into tumor hypoxia mechanisms have been hindered by the lack of intravital imaging tools capable of multiparametric probing of entire solid tumors with high spatial and temporal resolution. Here, we exploit volumetric multispectral optoacoustic tomography (vMSOT) for accurate, label-free delineation of tumor heterogeneity and dynamic oxygenation behavior. Mice bearing orthotopic MDA-MB-231 breast cancer xenografts were imaged noninvasively during rest and oxygen stress challenge, attaining time-lapse three-dimensional oxygenation maps across entire tumors with 100 µm spatial resolution. Volumetric quantification of the hypoxic fraction rendered values of 3.9% to 21.2%, whereas the oxygen saturation (sO_2) rate declined at 1.7% to 2.3% per mm in all tumors when approaching their core. Three distinct functional areas (the rim, hypoxic, and normoxic cores) were clearly discernible based on spatial sO_2 profiles and responses to oxygen challenge. Notably, although sO_2 readings were responsive to the challenge, deoxyhemoglobin (HbR) trends exhibited little to no variations in all mice. Dynamic analysis further revealed the presence of cyclic hypoxia patterns with a 21% average discrepancy between cyclic fractions assessed via sO_2 (42.2% ± 17.3%) and HbR fluctuations (63% ± 14.1%) within the hypoxic core. These findings corroborate the strong potential of vMSOT for advancing preclinical imaging of cancer and informing clinical decisions on therapeutic interventions.

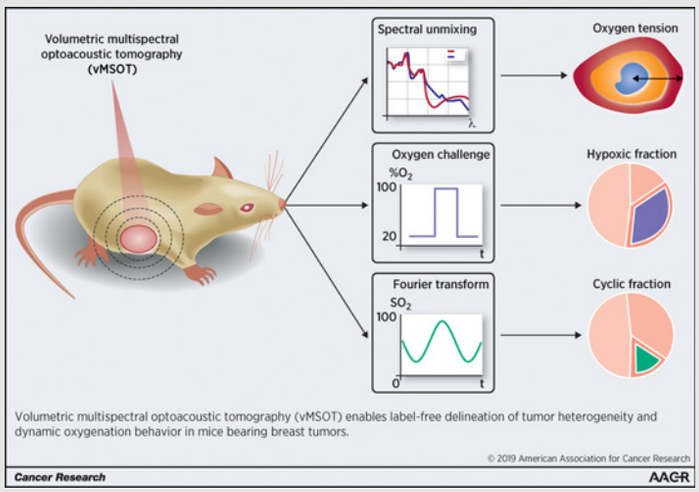

Significance: vMSOT provides quantitative measures of volumetric hypoxic fraction and cyclic hypoxia in a label-free and noninvasive manner, providing new readouts to aid tumor staging and treatment decision making.

Graphical Abstract: http://cancerres.aacrjournals.org/content/canres/79/18/4767/F1.large.jpg.

See related commentary by Klibanov and Hu, p. 4577

Introduction

Mapping tumor heterogeneity is a key approach for assessing the long-term responses to therapy (1). The physiologic microenvironment of neoplastic lesions is dictated by abnormal metabolism and neovascularization, differing substantially from healthy tissues. A particularly important alteration is the presence of hypoxia, a condition of reduced level of oxygen partial pressure (pO_2) during which cells undertake key biological pathways associated to tumor growth. It appears that tumors exhibit highly heterogeneous and dynamic oxygenation patterns, ranging from normoxia to hypoxia. Disorders in oxygen distribution can further results in significant variations in perfusion to neighboring regions (2). This apparently chaotic behavior of cancerous tissues represents a major obstacle for understanding the disease (3).

[1]Institute for Biological and Medical Imaging, Helmholtz Center Munich, Neuherberg, Germany. [2]Faculty of Medicine, Technical University of Munich, Munich, Germany. [3]Faculty of Medicine and Institute of Pharmacology and Toxicology, University of Zurich, Zurich, Switzerland. [4]Department of Information Technology and Electrical Engineering, Institute for Biomedical Engineering ETH Zurich, Zurich, Switzerland.

Note: Supplementary data for this article are available at Cancer Research Online (http://cancerres.aacrjournals.org/).

Corresponding Author: Daniel Razansky, Institute of Biomedical Engineering, University and ETH Zurich, Wolfgang-Pauli-Str. 27, 8093 Zurich, Switzerland. Phone: 41-44-633-3429; E-mail: daniel.razansky@uzh.ch

Cancer Res 2019;79:4767–75

doi: 10.1158/0008-5472.CAN-18-3769

Published OnlineFirst May 16, 2019; DOI: 10.1158/0008-5472.CAN-18-3769

Tumor hypoxia is also closely associated with resistance to chemotherapy and radiation therapy (4).

To this end, the spatial distribution of pO_2 within the tumor has been profiled via invasive methods, such as CT-guided pO_2 sensors. This enabled assessing the pO_2 drop between the viable rim and the core in just a few isolated locations (5). Imaging with ^{19}F-magnetic resonance oximetry (6) and ^{18}F-fluoromisonidazole PET (7) may provide higher spatial resolution but relies on exogenous oxygenation-sensitive agents. Furthermore, those methods mainly reveal static oxygenation profiles, only comprising a partial picture of the complex tumor microenvironment, while studying the transient spatiotemporal characteristics is essential for advancing the knowledge (8). For this, dynamic oxygen challenge has been suggested as a method for studying the oxygen stress response in tumors (9), aiming at characterizing the low perfusion efficiency of neovasculature by assessing responses to rapid respiratory challenges in different tumor subregions. Those were prominently studied with MRI (10) by exploiting the sensitivity of R_1-based sequences to changes of dissolved O_2 in blood (11). The approach was however limited by a relatively low spatiotemporal resolution further representing an indirect oxygen tension measure. It has been now widely recognized that, in addition to chronic hypoxia, reduced perfusion in some regions of the tumor may lead to appearance of hypoxic–reoxygenation periods. These fluctuations between hypoxic and nonhypoxic states are referred to as cyclic (dynamic) hypoxia (8), which is associated with increased tumor aggressiveness, resistance to treatments, and metastasis (12, 13). Hence, the ability to map and characterize the dynamics of cyclic heterogeneities may eventually contribute to improving treatment outcomes (14). Almost exclusively, MR methods have been used for this purpose. Although pO_2 and deoxyhemoglobin (HbR) variations were detected in tumor-bearing mice with electron paramagnetic (15) and with T2*-weighted (16) and R_2*-weighted (17) MRI, low spatiotemporal resolution remains the main limitation of MR-based methods preventing effective analysis of cyclic patterns in whole tumors. Moreover, conventional MRI instruments are restricted to HbR-correlated measurements lacking the clinical relevance of pO_2 (18). New methods to probe the tumor microenvironment over different time scales, from perfusion dynamics to neovasculature development, are then required for a better understanding of the processes involved in cancer progression.

Multispectral optoacoustic tomography (MSOT) is increasingly used in cancer research due to its unique capability for label-free noninvasive monitoring of hemodynamic parameters (19). A number of specific contrast agents have been further devised to sense key cancer biomarkers (20). MSOT was used to follow tumor growth and vascular development (21), to image tumor heterogeneity and perfusion (22–25), and to assess anticancer therapy efficacy (26). Previous works were yet limited to cross-sectional (2D) investigations unsuitable for an accurate characterization of differential real-time responses of neighboring subregions across entire solid tumors. Here we used instead a volumetric multispectral optoacoustic tomography system (vMSOT) approach based on simultaneous optoacoustic signal detection by a spherical array (27), with the aim to noninvasively characterize dynamic high-resolution patterns of acute and cyclic hypoxia in murine breast cancer models.

Materials and Methods

vMSOT

The vMSOT system is based on a previously described real-time volumetric tomography technique (28). Briefly, ultrasound (pressure) signals are induced by short (<10 ns duration) pulses of light from an optical parametric oscillator laser tunable in the near-infrared (NIR) spectral range (680–950 nm). The optoacoustically-generated signals are simultaneously detected by a 512-element spherical array transducer having 10 MHz detection bandwidth (Fig. 1A). During the experiments, the light fluence at the mouse skin surface was maintained below 20 mJ/cm^2 for all wavelengths. The system renders an effective field of view (FOV) of $6 \times 6 \times 6$ mm^3 with nearly isotropic three-dimensional (3D) spatial resolution in the 80 to 150 μm range. For imaging, both the transducer and the mouse were immersed in a water tank to facilitate propagation of the optoacoustically-generated pressure waves. Reconstruction of individual volumetric image frames for each illumination wavelength was performed with a graphics processing unit (GPU) implementation of a back-projection formula (29).

In vivo animal handling

The mouse *in vivo* experiments were approved by the government of Upper Bavaria. All experiments were performed in full compliance with the institutional guidelines of the Helmholtz Center Munich. Orthotopic tumors were induced in 6 weeks old female immunodeficient SHrN hairless NOD-SCID mice (Envigo) by subcutaneous injection of 3 million MDA-MB-231 cells in a total volume of 80 μL of PBS and Matrigel (1:1, v/v) into the inguinal gland of the mammary fat pad. *In vivo* imaging experiments were performed 30 days after cell inoculation, when the tumor reached an approximate size of 8 mm. The MDA-MB-231 cells were supplied by ATCC in May 2015, providing cell line authentication by STR analysis. The cell type was mycoplasma tested by a mycoplasma detection kit (Lonza) in March, 2019. Cells were used at four passages from thawing from frozen stocks. During acquisition, the mice were anesthetized with isoflurane [3% (v/v) for induction; 1.5%–2.0% (v/v) during imaging] in 100% O_2. A custom-made holder was used to maintain the mice in a stationary position with their fore and hind paws attached to the holder during the experiments. The mice were then immersed inside the water tank with the head kept outside water. The temperature of the water tank was maintained at 34°C with a feedback controlled heating stick. A breathing mask with a mouth clamp was used to fix the head in an upright position and to supply anesthesia and oxygen.

Whole tumor imaging and analysis

Although the effective FOV of the spherical array already covers a major portion of the tumor volume, high-resolution imaging of entire tumors and their surrounding areas was achieved by raster-scanning the array in the lateral (x–z) plane (Fig. 1A). Signal acquisition at multiple wavelengths (420, 730, 760, 800, and 850 nm) was performed to allow for a high-quality anatomical and functional tumor profiling. At each position of the array, 100 volumetric frames per wavelength were averaged after applying a motion rejection algorithm that eliminated frames affected by breathing-related motion (30). The reconstructed volumes were combined into a large-scale image of the entire region of interest (Fig. 1A). Images acquired at multiple

Published OnlineFirst May 16, 2019; DOI: 10.1158/0008-5472.CAN-18-3769

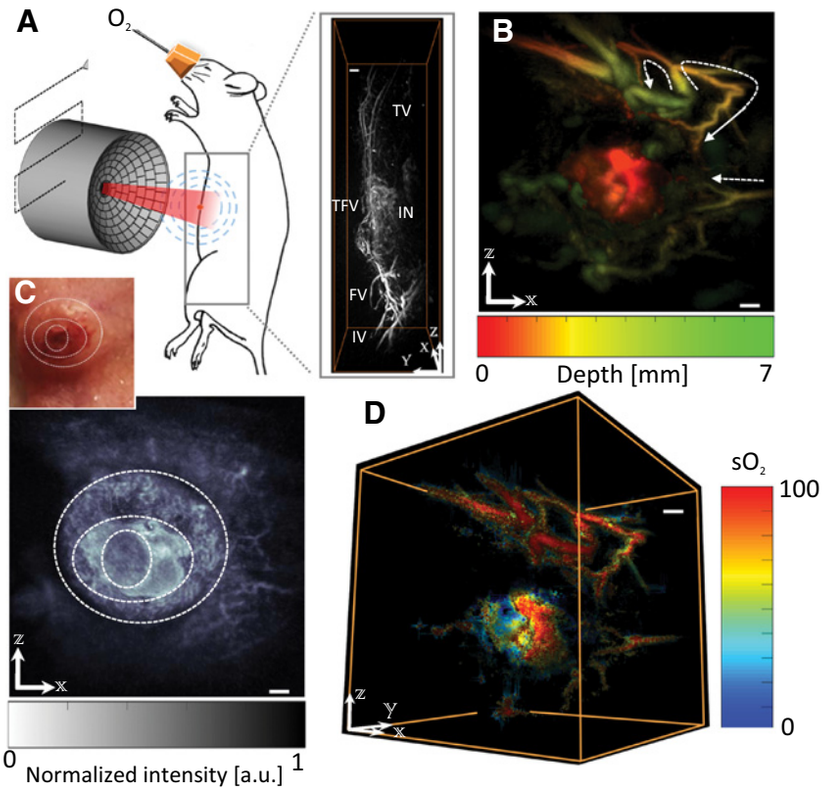

Figure 1.

A, Simplified schematic of the imaging set-up. The volumetric multispectral optoacoustic data were recorded with a spherical matrix array transducer probe that was also translated to acquire images from larger field of view. A typical 3D image of the thorax and abdominal region acquired at 800 nm from a tumor-bearing mouse is shown on the right. **B,** A zoomed-in depth encoded image of the tumor area showing vessel recruitment toward the core (white arrows). **C,** Photo of the tumor and a volumetric optoacoustic image (maximum intensity projection along *y*-axis) acquired at 420 nm. Three separate layers of dermis, rim, and core are visible. **D,** Spectrally unmixed sO_2 image of the same tumor showing the presence of hypoxic core and its highly oxygenated feeding vessels. Scale bar, 1 mm. a.u., arbitrary unit; FV, femoral vessels; IN, intestine; IV, ischiatic vessels; TFV, tumor feeding vessels; TV, thoratic vessels.

wavelengths were then processed with a standard linear unmixing method to estimate, on a voxel-per-voxel basis, the distribution of oxyhemoglobin (HbO), HbR, and total hemoglobin (THb) as well as the oxygen saturation (sO_2; ref. 31). 3D visualization of the optoacoustic images was done with Amira (Visual Sciences Group).

Segmentation into functional subregions

Tumors were segmented into 3 subregions, namely, the rim, normoxic, and hypoxic cores ($n = 6$ mice). The segmentation between the tumor rim and its core was done manually by estimating the boundary between the linear and parabolic-shape portions of the oxygen saturation profiles at 100% O_2 level, rendering boundary sO_2 values in the 50% to 62% range (Supplementary Fig. S1). The segmentation between the normoxic and hypoxic cores was based upon critical O_2 tension range of 10 to 20 mmHg pO_2 for which binding of hypoxia markers occurs (32). Note that the upper pO_2 threshold of 20 mmHg corresponds to a sO_2 value of 18% according to the Kelman and Severinghaus model (33) of the oxygen dissociation curve (where $pCO_2 = 40$ mmHg, pH 7, $T = 37°C$). Voxels with sO_2 values below 18% were thus regarded as hypoxic. The volumetric hypoxic fraction (vHF) measure was further calculated as the fraction of hypoxic voxels relative to the total voxel count in the tumor (voxels with insufficient signal-to-noise ratio were excluded).

Analysis of tumor dynamics

Dynamic tumor responses to breathing gas challenge were analyzed by recording time-lapse multispectral data with the spherical array remaining in a stationary position. The oxygen challenge experiments were performed by changing the percentage of oxygen in the breathing gas in the following order: 5 minutes of 20% O_2 (first baseline), 25 minutes of 100% O_2, and 15 minutes of 20% O_2 (second baseline). Prior to the challenge, the animals were given 15 minutes to stabilize at 20% O_2. To correct for respiratory motion artifacts, data were averaged over 2 seconds. Spatiotemporal volumetric sO_2 map was then calculated. Differential responses (ΔsO_2) to the oxygen stress were calculated on a per-voxel basis as signal difference between the averaged sO_2 during 100% O_2 breathing levels and the baselines, namely, each gas challenge yielded two differential responses for the first and second baselines. The ΔsO_2 voxels were grouped according to the 3 subregions, that is rim, normoxic core, and hypoxic core.

Cyclic hypoxia analysis

The second segment of the dynamic oxygen challenge corresponding to 25 minutes of 100% oxygen level was used for assessing cyclic hypoxia in the tumors of $n = 6$ mice. The analysis procedure is described elsewhere (34, 35). Briefly, the following processing steps were applied to the time profiles of each voxel: (i) linear detrending; (ii) calculation of the autocovariance; (iii) calculation of the power spectral density via fast Fourier transform (FFT); and (iv) thresholding according to a confidence interval, assuming that the signal is affected by Gaussian noise. Following these steps, the peak of the power spectrum for each voxel was identified. Voxels having a peak within frequency band of 0 to 0.005 Hz were regarded as cyclic voxels (3–18 cycles per hour is considered the relevant physiologic range; refs. 34, 36). The volumetric cyclic fraction (vCF) was calculated as the ratio

Published OnlineFirst May 16, 2019; DOI: 10.1158/0008-5472.CAN-18-3769

between the number of cyclic voxels and the total voxel count (excluding noisy voxels).

Statistical analysis

A total of $n = 6$ animals were evaluated contributing 12 independent ΔsO_2 measurements. For each subregion (rim, normoxic, or hypoxic core), approximately 100,000 voxels were evaluated. To represent the entire distribution for each subregion, pixels values were integrated using an average of all the pixels as well as the 25th percentile, median, and 75th percentile values. The differences in ΔsO_2 values across the subregions were compared using Friedman paired test followed by Dunn *post hoc* test. The differences between vCF values of the tumors ($n = 6$, calculated by either sO_2 or HbR analyses) were compared by an unpaired t test (*, $P < 0.05$; **, $P < 0.01$; ***, $P < 0.001$). Analyses were carried out using Matlab and SPSS 25.0 (SPSS Inc.).

Histologic validation

The mice were euthanized after being imaged with an overdose of ketamine (300 mg/kg) and directly stored at −80°C until performing whole body cryo-slicing. For this, the frozen specimen were embedded in Tissue-Tek O.C.T. compound (Sakura Finetech Europe). Ten-μm thick sections covering the entire tumor volume were extracted. IHC was performed on the frozen sections using antibodies against CD31 (Dianova) or CAIX (Novus Biologicals). Antibody staining was visualized with Alexa Fluor 488 or Alexa Fluor 594 conjugated secondary antibodies (Life Technologies, Thermo Fisher Scientific). All slices were further costained with 4',6-diamidino-2-phenylindole (DAPI; Molecular Probes, Thermo Fisher Scientific) to visualize cell bodies. Fluorescence compound slice images were recorded using an Imager M2, microscope (Carl Zeiss AG). Image acquisition and analysis was done using the Zeiss Zen 2 microscope software.

Results

Multispectral 3D tumor imaging

Position of the tumor in the inguinal mammary gland is clearly visible in the compounded volume image of the entire region surrounding the tumor, which was acquired by a large area scan of the mouse abdomen at 800 nm (Fig. 1A). Because of the relatively low light attenuation at this wavelength, both tumor core and vast recruitment of neovascular networks from as deep as 7 mm are clearly visible (Fig. 1B). Note also the direction of arrows indicating some feeding vessels that branch from larger vessels and propagate toward the core. Image acquired at 420 nm reveals a different sort of anatomical information (Fig. 1C). For this wavelength, hemoglobin and melanin are highly absorbing, hence superior vascular contrast is achieved to the detriment of the maximal penetration depth of approximately 2 mm. Three distinct ring-type patterns can be observed across the tumor surface matching the photograph (Fig. 1C). An outer ring of epidermal and dermal layers is characterized by melanin absorption and fine vasculature patterns of the larger venules and arterioles (37). The middle ring with strong absorption signals is attributed to a highly oxygenated rim layer located close to the surface. Finally, the inner ring belongs to the tumor core that breaches the dermal layer and is characterized by reduced signal intensity. The sO_2 map retrieved from the multispectral data at 730, 760, 800, and 850 nm (Fig. 1D) suggests that the feeding vessels are well oxygenated whereas the core appears to be at an advanced hypoxic state with the highly perfused region at the edge, arguably belonging to the rim.

Analysis of the spatial sO_2 profiles

Spatial profiling of tumor oxygenation was performed by analyzing selected coronal slices at different depths (Fig. 2A). In this way, high-resolution sO_2 variations could be calculated as a function of distance from the center of the tumor (Fig. 2B). The corresponding sO_2 profiles (Fig. 2C; Supplementary Fig. S1) exhibit a substantial difference between the outer rim and the core with an average sO_2 drop of 1.7% to 2.3% per mm, as estimated by linear fitting. Segmentation of the rim and the core regions was based on thresholding the spatial sO_2 profiles, as shown for an exemplary slice in Fig. 2C. Comparison of the sO_2 map acquired at approximately 2 mm depth *in vivo* (Fig. 2D) with its corresponding *ex vivo* IHC showed that high sO_2-values colocalize with high expressions of CAIX (Fig. 2E) and CD31 (Fig. 2F), which may indicate that both proteins facilitate enhanced oxygen supply to the rim. Note, however, that both CAIX and CD31 can also be found in the tumor core, although with less confinement and lower density as compared with the rim.

Oxygen challenge responses

Owing to their disparate perfusion patterns, it is generally anticipated for the distinct tumor subregions to exhibit different responses to the dynamic oxygen challenge. As described in the previous section, the rim and core of each tumor were discerned by analyzing their corresponding spatial sO_2 profiles. Inside the core, a further segmentation into hypoxic and normoxic subregions was established via threshold-based approach by considering the critical O_2 tension for which binding of hypoxia markers occurs. Three distinct hypoxic foci are visible in a central sagittal slice showing the spatial architecture of neighboring hypoxic and normoxic subregions (Fig. 3A). A quantitative analysis of the relative volumes of the regions (Supplementary Table S1) allows for a more accurate assessment of hypoxia progression in the tumor. The relative volumetric fraction of the subregions was similar among all the imaged tumors, as well as the calculated vHFs (3.9–21.2%).

Additional insights on oxygen transport to the 3 subregions can be drawn by observing local sO_2 responses to the oxygen challenge (Fig. 3B; Supplementary Fig. S2) as well as the time-lapse video of the responses in single voxels (Supplementary Video S1). In all tumors, the rim and the normoxic core exhibit rapid response onset times of 1 to 2 minutes followed by a steady baseline. In contrast, hypoxic regions in the core exhibit moderate and unstable drops. These responses are not at all visible in the corresponding THb trends (Fig. 3C), which are characterized by a relative plateau in all tumors. The measured values of absolute sO_2 difference (ΔsO_2) between the baseline and 100% oxygen phase further show that each subregion presents a distinct response to the oxygen stress challenge (Fig. 3D; Supplementary Fig. S3), which held true for all the imaged tumors. Paired comparisons between the subregions of each tumor indicated that segregation between rim, normoxic core and hypoxic core is statistically significant across all the measurements ($P < 0.05$).

Published OnlineFirst May 16, 2019; DOI: 10.1158/0008-5472.CAN-18-3769

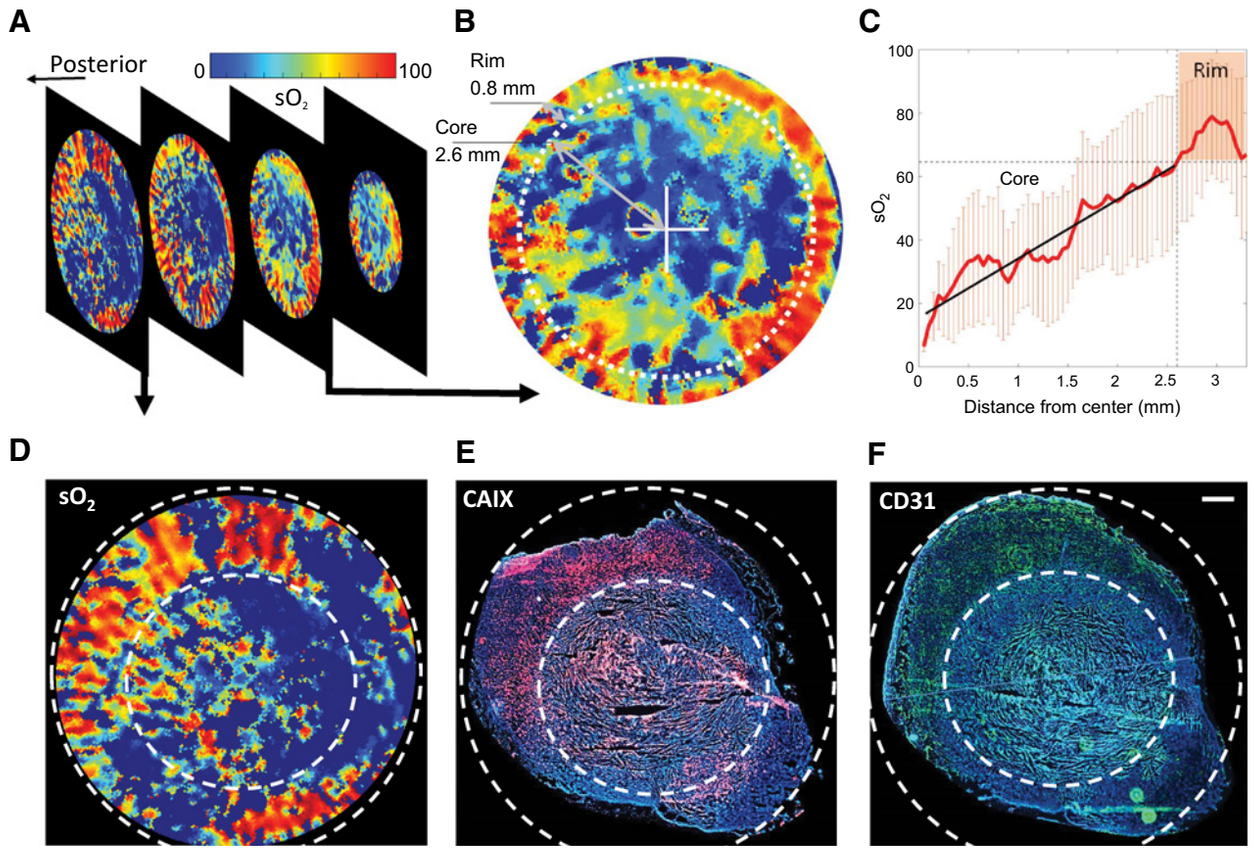

Figure 2.

A, A 3D stack of coronal slices extracted from the volumetric sO_2 map of the tumor. **B,** A representative slice showing the presence of two distinct tumor subregions. **C,** Radial sO_2 profile as a function of the distance from the tumor core ($R^2 = 0.78$). The calculated border between the rim and core is labeled by a dashed line. **D–F,** *In vivo* sO_2 map (**D**) of a different slice with its corresponding CAIX-DAPI histopathology (**E**) and CD31-DAPI staining (**F**) qualitatively matching the regions of enhanced oxygen supply and reduced oxygen supply. Scale bar, 1 mm.

Cyclic hypoxia

We subsequently exploited the unique rapid volumetric multispectral imaging capabilities of the vMSOT system in order to assess cyclic hypoxia patterns by comparing periodic variations of HbR and sO_2. HbR is of particular interest because it directly corresponds to the commonly measured BOLD MRI signals. The frequency spectrum of the HbR signal from a typical voxel in a central sagittal slice through a tumor exhibits a dominant frequency at 0.001 Hz (Fig. 4A). This value corresponds to 3 to 4 cycles per hour and was in fact predominantly manifested in majority of the tumor mass in all measurements, both in the unmixed HbR and sO_2 signal channels (Fig. 4A). The fluctuations of sO_2 and HbR have a characteristic amplitude variation of nearly 30% (Fig. 4B). We estimated the vCF values in all the imaged tumors to be in the 17% to 59% range (Supplementary Table S2), resembling the pO_2 ranges of 13% to 52% reported for ^{18}F-miso PET (38) and of 21 ± 6% to 41 ± 3% as measured by EPRI (15). An average discrepancy of 14% was observed between vCFs calculated from the HbR variations versus those based on the sO_2 (Fig. 4C). Notably, the hypoxic core subregion yielded the most significant difference ($P < 0.05$).

Discussion

Importance of mapping the spatial distribution of pO_2 in solid tumors has been acknowledged ever since hypoxia has been linked to treatment outcomes (1). Herein, we provided unique estimates of the 3D distribution of oxygenation patterns in murine breast cancer models with excellent spatial and temporal resolution owing to the new vMSOT approach. The imaging system provides sO_2 values by unmixing of multispectral data, from which the equivalent pO_2 can be calculated. We exploited the unique capabilities of vMSOT to gather otherwise unattainable information on the static, dynamic and cyclic sO_2 behavior in distinct tumor subregions. Experiments in mice implanted with MDA-MB-231 tumor cells indicated that sO_2 linearly increases by 1.7% to 2.3% sO_2 per mm when moving away from the center of the core. This constitutes a useful metric for accurate assessment of the tumor perfusion and matureness (23). Volumetric quantification of hypoxic fraction rendered a similar range of 12.2 ± 6.5% in all the studied tumors. This parameter was previously suggested for guiding clinical decisions pertaining optimization of tumor therapies (39). In this regard, the truly volumetric information provided by vMSOT is expected to

Published OnlineFirst May 16, 2019; DOI: 10.1158/0008-5472.CAN-18-3769

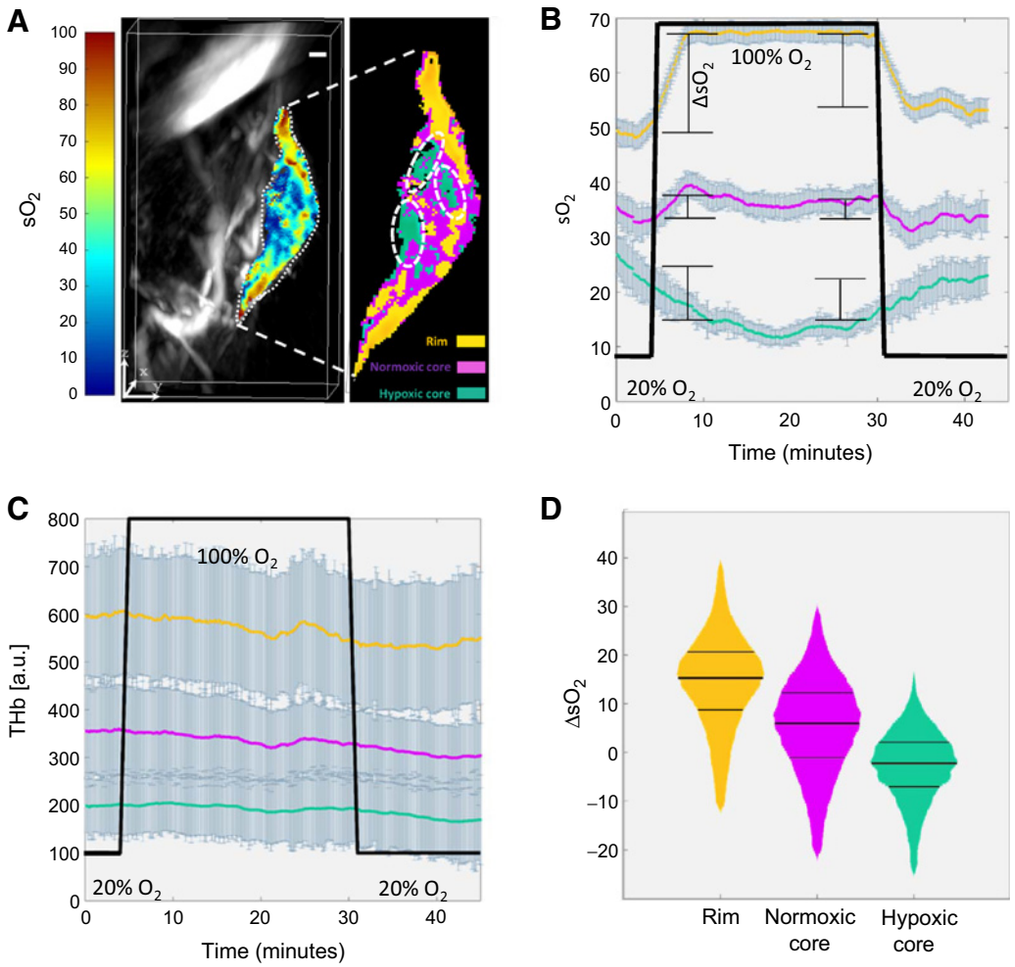

Figure 3.

A, sO_2 map of a sagittal slice of the tumor superimposed on an anatomical (single wavelength) optoacoustic image. Segmentation into three subregions (rim, normoxic core, and hypoxic core) is shown in the zoom-in. Scale bar, 1 mm. **B,** Average (with 1 SD) sO_2 response of each subregion to the dynamic oxygen challenge of a single animal (mouse #1). **C,** The corresponding THb signal exhibiting no significant variations in response to the oxygen challenge. **D,** The corresponding voxel distribution plot presenting the percentile differences between the oxygen saturation for 100% and 20% O_2 (center line represents the median, whereas the top and bottom thresholds represent the 25th and 75th quartiles). a.u., arbitrary unit.

significantly increase its accuracy with respect to 2D imaging approaches.

Here we were able to segment the tumor into 3 subregions, namely the rim, hypoxic, and normoxic cores. Although the rim area was subjectively differentiated by relying on its distinct features in the spatial sO_2 profiles, the core was segmented into hypoxic and normoxic subregions based on a theoretical threshold of critical pO_2 for which binding of hypoxia markers occurs. Note that translation between pO_2 and sO_2 according to the oxygen dissociation curves might be prone to errors due to variability in the temperature, pCO_2, or pH. The effectiveness of our segmentation methodology was further substantiated by demonstrating that oxygen saturation of the tumor subregions is significantly different. It is long known that chronic hypoxia in tumors is closely associated with limited perfusion (2). Thereby, we hypothesized that a dynamic oxygen challenge would correspondingly reveal different local responses among the subregions. This was tested by exploiting the unique real-time 3D imaging capabilities of the vMSOT system. Notably, the ΔsO_2 analysis yields a good distinction ($P < 0.05$) between the subregions in all mice. It was shown that the rim and the normoxic subregions of the core exhibited significant variations in response to the oxygen stress, whereas the sO_2 in the hypoxic core decreased only mildly. Note that declining sO_2 trends during oxygen stress have been previously reported in prostate tumor cores (23). It is also worth mentioning that although sO_2 was responsive to the challenge, THb was barely altered in all mice. This indicates a clear advantage of the method with respect to alternative imaging modalities unable to differentiate between the oxygenated and deoxygenated states of hemoglobin. The dynamic ΔsO_2 analysis was thus exploited as a new robust method for direct segmentation of tumor subregions, which can be used to complement

Published OnlineFirst May 16, 2019; DOI: 10.1158/0008-5472.CAN-18-3769

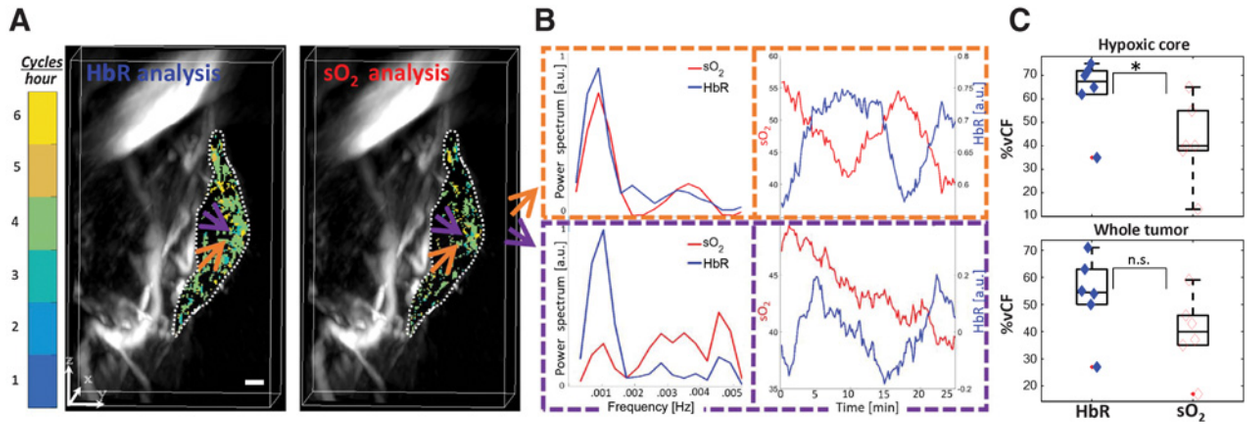

Figure 4.

A, Frequency map (single slice) of the hypoxic cycles in the tumor, as analyzed by HbR fluctuations and sO_2 fluctuations. The HbR-based maps exhibit higher density of cyclic voxels in comparison with the sO_2-based maps. Scale bar, 1 mm. **B,** Power spectrum and the corresponding amplitude fluctuations of two representative voxels. One voxel (orange arrow in **A**) exhibits cyclic behavior in both HbR and sO_2 channels, whereas the voxel labeled by a purple arrow only manifests cyclic behavior in the HbR channel. **C,** Distribution of vCF in all tumors reveals significant differences between the sO_2- and HbR-based analyses ($n = 6$). a.u., arbitrary unit; n.s., not significant. *, $P < 0.05$.

measurements done by other modalities that do not measure pO_2 or sO_2 directly but can only observe changes in trends (e.g., BOLD-MRI). Yet, it should be noted that the accuracy of sO_2 quantification by vMSOT might be affected by wavelength-dependent light attenuation in heterogeneous tissues (40, 41). For this reason, ΔsO_2 represents a more robust metric capable of eliminating common biases. The lack of variations in the THb profiles may be attributed to the limited vasoconstriction effects and the vascular tone within tumors (42, 43), which may further diminish due to the generally low levels of vessels functionality in MDA-MB-231 tumors (44).

Hemoglobin is an intrinsic contrast molecule for BOLD-MRI, which has been previously used for noninvasive characterization of cyclic hypoxia. The latter is known to have physiologic effects different from those of acute hypoxia (8). Our study is the first to detect the presence of cyclic hypoxia optoacoustically. We were able to analyze the cyclic oscillations of sO_2 and HbR simultaneously by solely relying on endogenous contrast. vMSOT provided a volumetric analysis of the entire tumor volume at high spatial and temporal resolution, which may contribute to an enhanced reliability of the cyclic fraction estimations. We observed discrepancy between the vCF values calculated via sO_2 versus HbR. On average, 14% of the tumor volume manifested cyclic hypoxia behavior in the HbR channel but not in the sO_2. Notably, the hypoxic core exhibited the highest vCF values. This is consistent with a previously reported observation that cyclic hypoxia is more likely to appear in tumor regions where oxygen saturation of the blood entering that region is relatively low (45). Moreover, the hypoxic core was also the region manifesting the most significant discrepancy of 21% between the sO_2 and HbR fluctuations. Because of the close relationship between sO_2 and pO_2, these results suggest an overestimation of cyclic fraction by the BOLD signal and other imaging methods solely using HbR-sensitive readouts for the cyclic analysis. Such a bias may have a clinical significance in treatment decisions that are based on the cyclic fraction values. MSOT has recently offered great prospects for clinical translation in the field of metastatic lymph node detection (46) and breast cancer diagnostics (47–49). Therefore, preclinical studies with vMSOT may inform clinical decisions by, for example, providing error estimates of the vCF measurements for different tumor types. The new imaging capabilities demonstrated in this work further foster optoacoustic imaging as a valuable tool for the screening, diagnosis, treatment planning, and monitoring of cancer.

Disclosure of Potential Conflicts of Interest

D. Razansky has ownership interest (including stock, patents, etc.) in and is a consultant/advisory board member of iThera Medical GmbH. No potential conflicts of interest were disclosed by the other authors.

Authors' Contributions

Conception and design: A. Ron, X.L. Deán-Ben, D. Razansky
Development of methodology: A. Ron, D. Razansky
Acquisition of data (provided animals, acquired and managed patients, provided facilities, etc.): A. Ron, X.L. Deán-Ben, S. Gottschalk, D. Razansky
Analysis and interpretation of data (e.g., statistical analysis, biostatistics, computational analysis): A. Ron, S. Gottschalk
Writing, review, and/or revision of the manuscript: A. Ron, X.L. Deán-Ben, S. Gottschalk, D. Razansky
Study supervision: D. Razansky

Acknowledgments

The authors wish to thank Z. Silman for her great support with biostatistics, M. Reiss for his support with the measurements and animals handling, and S. Glasl and U. Klemm for their valuable advice. This work was supported by the German Research Foundation research grant RA1848/5-1.

The costs of publication of this article were defrayed in part by the payment of page charges. This article must therefore be hereby marked *advertisement* in accordance with 18 U.S.C. Section 1734 solely to indicate this fact.

Received November 30, 2018; revised April 3, 2019; accepted May 10, 2019; published first May 16, 2019.

References

1. Vaupel P, Mayer A. Hypoxia in cancer: significance and impact on clinical outcome. Cancer Metastasis Rev 2007;26:225–39.
2. Gillies RJ, Schomack PA, Secomb TW, Raghunand N. Causes and effects of heterogeneous perfusion in tumors. Neoplasia 1999;1:197–207.
3. Vaupel P, Schlenger K, Knoop C, Höckel M. Oxygenation of human tumors: evaluation of tissue oxygen distribution in breast cancers by computerized O2 tension measurements. Cancer Res 1991;51:3316–22.
4. Liu C, Lin Q, Yun Z. Cellular and molecular mechanisms underlying oxygen-dependent radiosensitivity. Radiat Res 2015;183:487–96.
5. Gatenby R, Coia L, Richter M, Katz H, Moldofsky P, Engstrom P, et al. Oxygen tension in human tumors: in vivo mapping using CT-guided probes. Radiology 1985;156:211–4.
6. Heerschap A, Simonetti AW, Rijken PF, Peters HP, StB̈en G, van der Kogel AJ. Characterization and validation of noninvasive oxygen tension measurements in human glioma xenografts by 19F-MR relaxometry. Int J Radiat Oncol Biol Phys 1999;44:649–58.
7. O'Donoghue JA, Zanzonico P, Pugachev A, Wen B, Smith-Jones P, Cai S, et al. Assessment of regional tumor hypoxia using 18F-fluoromisonidazole and 64Cu (II)-diacetyl-bis (N4-methylthiosemicarbazone) positron emission tomography: comparative study featuring microPET imaging, Po2 probe measurement, autoradiography, and fluorescent microscopy in the R3327-AT and FaDu rat tumor models. Int J Radiat Oncol Biol Phys 2005;61:1493–502.
8. Michiels C, Tellier C, Feron O. Cycling hypoxia: a key feature of the tumor microenvironment. Biochimica Biophys Acta 2016;1866:76–86.
9. Zhao D, Pacheco-Torres J, Hallac RR, White D, Peschke P, Cerdán S, et al. Dynamic oxygen challenge evaluated by NMR T1 and T2*–insights into tumor oxygenation. NMR Biomed 2015;28:937–47.
10. Zhao D, Constantinescu A, Hahn EW, Mason RP. Differential oxygen dynamics in two diverse Dunning prostate R3327 rat tumor sublines (MAT-Lu and HI) with respect to growth and respiratory challenge. Int J Radiat Oncol Biol Phys 2002;53:744–56.
11. O'Connor JP, Boult JK, Jamin Y, Babur M, Finegan KG, Williams KJ, et al. Oxygen enhanced MRI accurately identifies, quantifies, and maps hypoxia in preclinical cancer models. Cancer Res 2016;76:787–95.
12. Daneau G, Boidot R, Martinive P, Feron O. Identification of cyclooxygenase-2 as a major actor of the transcriptomic adaptation of endothelial and tumor cells to cyclic hypoxia: effect on angiogenesis and metastases. Clin Cancer Res 2010;16:410–9.
13. Moeller BJ, Cao Y, Li CY, Dewhirst MW. Radiation activates HIF-1 to regulate vascular radiosensitivity in tumors: role of reoxygenation, free radicals, and stress granules. Cancer Cell 2004;5:429–41.
14. Matsumoto S, Yasui H, Mitchell JB, Krishna MC. Imaging cycling tumor hypoxia. Cancer Res 2010;70:10019–23.
15. Yasui H, Matsumoto S, Devasahayam N, Munasinghe JP, Choudhuri R, Saito K, et al. Low-field magnetic resonance imaging to visualize chronic and cycling hypoxia in tumor-bearing mice. Cancer Res 2010;70:6427–36.
16. Baudelet C, Cron GO, Ansiaux R, Crokart N, DeWever J, Feron O, et al. The role of vessel maturation and vessel functionality in spontaneous fluctuations of T2*-weighted GRE signal within tumors. NMR Biomed 2006;19:69–76.
17. Panek R, Welsh L, Baker LCJ, Schmidt MA, Wong KH, Riddell AM, et al. Noninvasive imaging of cycling hypoxia in head and neck cancer using intrinsic susceptibility MRI. Clin Cancer Res 2017;23:4233–41.
18. Baudelet C, Gallez B. How does blood oxygen leveldependent (BOLD) contrast correlate with oxygen partial pressure (pO_2) inside tumors? Magn Reson Med 2002;48:980–6.
19. Deán-Ben X, Gottschalk S, Mc Larney B, Shoham S, Razansky D. Advanced optoacoustic methods for multiscale imaging of in vivo dynamics. Chem Soc Rev 2017;46:2158–98.
20. Levi J, Kothapalli SR, Bohndiek S, Yoon JK, Dragulescu-Andrasi A, Nielsen C, et al. Molecular photoacoustic imaging of follicular thyroid carcinoma. Clin Cancer Res 2013;19:1494–502.
21. Laufer JG, Zhang EZ, Treeby BE, Cox BT, Beard PC, Johnson P, et al. In vivo preclinical photoacoustic imaging of tumor vasculature development and therapy. J Biomed Opt 2012;17:056016.
22. Tomaszewski MR, Gehrung M, Joseph J, Quiros-Gonzalez I, Disselhorst JA, Bohndiek SE. Oxygen-enhanced and dynamic contrast-enhanced optoacoustic tomography provide surrogate biomarkers of tumor vascular function, hypoxia, and necrosis. Cancer Res 2018;78:5980–91.
23. Tomaszewski MR, Gonzalez IQ, O'Connor JP, Abeyakoon O, Parker GJ, Williams KJ, et al. Oxygen enhanced optoacoustic tomography (OE-OT) reveals vascular dynamics in murine models of prostate cancer. Theranostics 2017;7:2900.
24. Herzog E, Taruttis A, Beziere N, Lutich AA, Razansky D, Ntziachristos V. Optical imaging of cancer heterogeneity with multispectral optoacoustic tomography. Radiology 2012;263:461–8.
25. Ermolayev V, Dean-Ben XL, Mandal S, Ntziachristos V, Razansky D. Simultaneous visualization of tumour oxygenation, neovascularization and contrast agent perfusion by real-time three-dimensional optoacoustic tomography. Eur Radiol 2016;26:1843–51.
26. Xie B, Tomaszewski MR, Neves A, Ros S, Hu DE, McGuire S, et al. Optoacoustic detection of early therapy-induced tumor cell death using a targeted imaging agent. Clin Cancer Res 2017;23:6893–903.
27. Deán-Ben XL, Fehm TF, Ford SJ, Gottschalk S, Razansky D. Spiral volumetric optoacoustic tomography visualizes multi-scale dynamics in mice. Light Sci Appl 2017;6:e16247.
28. Deán-Ben XL, Sela G, Lauri A, Kneipp M, Ntziachristos V, Westmeyer GG, et al. Functional optoacoustic neuro-tomography for scalable whole-brain monitoring of calcium indicators. Light Sci Appl 2016;5:e16201.
29. Rosenthal A, Ntziachristos V, Razansky D. Acoustic inversion in optoacoustic tomography: a review. Curr Med Imaging Rev 2013;9:318–36.
30. Fehm TF, Deán-Ben XL, Ford SJ, Razansky D. In vivo whole-body optoacoustic scanner with real-time volumetric imaging capacity. Optica 2016;3:1153–9.
31. Razansky D, Buehler A, Ntziachristos V. Volumetric real-time multispectral optoacoustic tomography of biomarkers. Nat Protoc 2011;6:1121.
32. Hockel M, Vaupel P. Tumor hypoxia: definitions and current clinical, biologic, and molecular aspects. J Natl Cancer Inst 2001;93:266–76.
33. Severinghaus JW. Simple, accurate equations for human blood O2 dissociation computations. J Appl Physiol 1979;46:599–602.
34. Baudelet C, Ansiaux R, Jordan BF, Havaux X, Macq B, Gallez B. Physiological noise in murine solid tumours using T2*-weighted gradient-echo imaging: a marker of tumour acute hypoxia? Phys Med Biol 2004;49:3389.
35. Baudelet C, Gallez B. Cluster analysis of BOLD fMRI time series in tumors to study the heterogeneity of hemodynamic response to treatment. Magn Reson Med 2003;49:985–90.
36. Gonçalves MR, Johnson SP, Ramasawmy R, Pedley RB, Lythgoe MF, Walker-Samuel S. Decomposition of spontaneous fluctuations in tumour oxygenation using BOLD MRI and independent component analysis. Br J Cancer 2015;113:1168.
37. Braverman IM. The cutaneous microcirculation: ultrastructure and microanatomical organization. Microcirculation 1997;4:329–40.
38. Wang K, Yorke E, Nehmeh SA, Humm JL, Ling CC. Modeling acute and chronic hypoxia using serial images of PET. Med Phys 2009;36:4400–8.
39. Wilson WR, Hay MP. Targeting hypoxia in cancer therapy. Nat Rev Cancer 2011;11:393.
40. Olefir I, Tzoumas S, Yang H, Ntziachristos V. A Bayesian approach to eigenspectra optoacoustic tomography. IEEE Trans Med Imaging 2018;37:2070–9.
41. Tzoumas S, Nunes A, Olefir I, Stangl S, Symvoulidis P, Glasl S, et al. Eigenspectra optoacoustic tomography achieves quantitative blood oxygenation imaging deep in tissues. Nat Commun 2016;7:2121.
42. Carpenter CM, Rakow-Penner R, Jiang S, Daniel BL, Pogue BW, Glover GH, et al. Inspired gas-induced vascular change in tumors with magnetic-resonance-guided near-infrared imaging: human breast pilot study. J Biomed Opt 2010;15:036026.
43. West JB. Respiratory physiology: the essentials. Baltimore, MD: Lippincott Williams & Wilkins; 2012.
44. Quiros-Gonzalez I, Tomaszewski MR, Aitken SJ, Ansel-Bollepalli L, McDuffus L-A, Gill M, et al. Optoacoustics delineates murine breast cancer models displaying angiogenesis and vascular mimicry. Br J Cancer 2018;118:1098.
45. Dewhirst MW. Relationships between cycling hypoxia, HIF-1, angiogenesis and oxidative stress. Radiat Res 2009;172:653–65.
46. Stoffels I, Morscher S, Helfrich I, Hillen U, Leyh J, Burton NC, et al. Metastatic status of sentinel lymph nodes in melanoma determined

noninvasively with multispectral optoacoustic imaging. Sci Transl Med 2015;7:317ra199.
47. Lin L, Hu P, Shi J, Appleton CM, Maslov K, Li L, et al. Single-breath-hold photoacoustic computed tomography of the breast. Nat Commun 2018;9: 2352.
48. Abeyakoon O, Morscher S, Dalhaus N, Ford SJ, Mendichovszky IA, Manavaki R, et al. Optoacoustic imaging detects hormone-related physiological changes of breast parenchyma. Ultraschall Med 2018 Jun 7 [Epub ahead of print].
49. Heijblom M, Piras D, van den Engh FM, van der Schaaf M, Klaase JM, Steenbergen W, et al. The state of the art in breast imaging using the Twente Photoacoustic Mammoscope: results from 31 measurements on malignancies. Eur Radiol 2016;26: 3874–87.

Published OnlineFirst May 16, 2019; DOI: 10.1158/0008-5472.CAN-18-3769

Cancer Research
The Journal of Cancer Research (1916–1930) | The American Journal of Cancer (1931–1940)

AACR American Association for Cancer Research

Volumetric Optoacoustic Imaging Unveils High-Resolution Patterns of Acute and Cyclic Hypoxia in a Murine Model of Breast Cancer

Avihai Ron, Xosé Luís Deán-Ben, Sven Gottschalk, et al.

Cancer Res 2019;79:4767-4775. Published OnlineFirst May 16, 2019.